Hydrogen oxidation pathway over ni–ceria electrode: combined study of dft and exp…

Health & Medicine

Introduction

As a device that efficiently transfers chemical fuel energy into electricity, solid oxide fuel cell (SOFC) is given a competitive edge in long-term stability, fuel flexibility, and sustainable energy in the future (Ormerod, 2003). One of the key steps in the electrochemical energy conversion process is the fuel oxidation reaction at the anode, where the fuel molecule such as H_2 and CO combines with an oxygen ion $O_O^\times$ meanwhile releasing electrons and forming an oxygen ion vacancy $V_O^{\bullet\bullet}$. In the case where hydrogen or reform gas is supplied as the fuel, the hydrogen oxidation reaction at the anode can be written as Equation (1).

$$H_2(g) + O_O^\times \rightarrow H_2O(g) + V_O^{\cdot\cdot} + 2e' \quad (1)$$
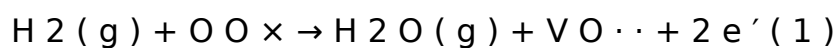
The equation shows that the anodic reaction usually takes place at the three-phase boundaries (3PB), where the fuel gas, the electrons, and oxygen ions are all available (Sun and Stimming, 2007). This is the case for the state-of-the-art Ni–yttrium-stabilized zirconia (YSZ) cermet anodes, which have been widely used in intermediate- and high-temperature SOFCs that operate at temperature up to 1, 000°C (Horita et al., 2006). In the Ni–YSZ cermet, the reaction occurs only at the Ni–YSZ–gas 3PB since YSZ is a pure oxygen ion conductor that transport oxygen ions and oxygen vacancies while metallic nickel plays the role of both electronic conductor and electrocatalyst.

Different from YSZ, ceria-based oxygen ion conductors also have electronic conductivities due to the facile conversion between Ce^{3+} and Ce^{4+} oxidation states in the anodic conditions of low oxygen partial pressure and

high temperature. The variable oxidation state dedicates ceria to catalyze the fuel oxidation reaction and facilitates the formation of additional oxygen vacancies. The character of mixed conductivity makes it possible to electrochemically oxidize the fuel on the ceria surfaces. Thus, replacing zirconia with ceria will extend the reaction sites from 3PB to the whole surface of the cermet anode within the effective reaction zone and consequently increase the electrode performance. In addition, the oxygen ionic conductivities of ceria-based electrolytes such as samaria-doped ceria (SDC) are several times higher than those of zirconia-based electrolytes like YSZ. The high conductivity increases the availability of oxygen ions, thus enlarging the electrochemically effective zone. Comprehensively, compared with Ni–YSZ, ceria-based cermets exhibit much higher anodic activity, especially at intermediate temperatures below 800°C (Kašpar et al., 1999 ; Fergus, 2006). Besides, when hydrocarbon fuel is supplied to the anode, Ni–ceria cermets show higher resistance to carbon deposition than Ni–YSZ since carbon can be removed through combining with oxygen from ceria due to the capability of changing oxidation states (Ramirez-Cabrera et al., 2000 ; Laosiripojana et al., 2005).

While Ni–ceria shows many advantages, its anode reaction mechanism is not understood as clearly as that of Ni–YSZ. Hydrogen oxidation occurs only at the 3PB in the system of Ni–YSZ, and the kinetic pathway for such reaction could be subdivided into three parts: hydrogen adsorption on Ni, hydrogen spillover to the Ni–YSZ interface, and water formation and desorption at 3PB (Shishkin and Ziegler, 2009 ; Cucinotta et al., 2011). For the Ni–ceria cermets, the reaction takes place not only at 3PB but also at the ceria

surface due to the higher availability of surface oxygen vacancy. By comparing the electronic properties of Ni–YSZ and Ni–CeO$_2$ interfaces, Shishkin and Ziegler demonstrate that the formation of the surface vacancy is much easier in the case of Ni–CeO$_2$, while oxygen vacancy can only exists at 3PB for Ni–YSZ (Shishkin and Ziegler, 2014). Calculation on Ni–CeO$_2$ (111) system reveals that the surface oxygen vacancy is energetically more favored than the interfacial oxygen vacancy (Shishkin and Ziegler, 2010a). Furthermore, Hahn et al. suggest that oxygen vacancy is affected by the position of reduced Ce^{3+} sites in CeO$_2$ and the quantum number of their occupied f-type orbitals (Hahn et al., 2015). Although some properties in Ni–CeO$_2$ system are studied through theoretical calculations, the overall reaction pathway of hydrogen oxidation is still uncovered. In this work, we adopt density functional theory with strong correlated correction (DFT + U) method to evaluate different molecular pathways of H$_2$ oxidation on Ni–CeO$_2$ (111) surface. Possible H$_2$ oxidation mechanisms with different pathways is unveiled and demonstrated systematically. The energetically favored pathway is concluded from theoretical calculations and further shown *via* experimental approaches.

Computational Methods

All spin-polarized calculations were accomplished by DFT method implemented in the Vienna *ab initio* simulation package (VASP) (Kresse and Furthmüller, 1996). The generalized gradient approximation (GGA) with the Perdew–Burke–Ernzerhof (PBE) functional was used (Blochl et al., 1994 ; Perdew et al., 1996 ; Hammer et al., 1999). To accurately describe the strongly corrected electrons of the localized Ce 4f orbitals, GGA + U with U

$_{eff}$ = 5 eV for Ce ions was adopted (Nolan et al., 2005 ; Andersson et al., 2007). The projector-augmented wave (PAW) method was carried out to deal with the interaction between ionic core electrons and valence electrons with Ce([Xe]4f ^{1} 5d ^{1} 6s ^{2}), Ni([Ar]3d ^{8} 4s ^{2}), O(1s ^{2} 2s ^{2} 2p ^{4}), and H(1s ^{1}) (Blochl et al., 1994 ; Perdew et al., 1996). The force on atom was smaller than 0. 03 eV/Å for the geometric optimization. It was set at 400 eV for the kinetic energy cutoff and the convergence criteria was 10 $^{-4}$ eV for the electronic structure calculations. The low-index (111) surface of CeO $_2$ is the most stable surface, which was selected as the substrate (Conesa, 1995).

On the basis of the Monkhorst–Pack scheme, the Brillouin zone was sampled with a 6 × 6 × 6 k -point grid for CeO $_2$ bulk. The optimized lattice parameter of ceria was 5. 437 Å, consistent with the experimental result of 5. 411 Å (Kümmerle and Heger, 1999). The CeO $_2$ (111) with a 4 × 4 slab was simulated by using two O–Ce–O triple layers of which atoms in the bottom O–Ce–O layer were fixed as their bulk positions. The thickness of vacuum was set to 15 Å to avoid the interslab interaction between two neighboring slabs along the direction perpendicular to the surface. The Ni $_{10}$ cluster and the bond lengths of the H $_2$ and O $_2$ molecules have been previously optimized within a 15-Å cubic box. The evaluated that the bond lengths of the H $_2$ and O $_2$ molecule agree with our previous research (Wang et al., 2016). The energy of triple oxygen was utilized for all the calculations. The detailed location of H $_2$ oxidation reaction and energy of the transition state (TS) were simulated with the climbing image nudged elastic band (CI-NEB) method. In the reaction pathway diagrams (Figures 3 – 6), ΔE_x represents the energy

difference of structures between two neighboring reaction stages, which is equal to the energy of the x th stage minus the energy of the previous stage. ΔE_{TSx} represents the energy barrier of the transition state.

Experimental

Electrical Conductivity Relaxation Measurement

The reaction kinetics was measured using the electrical conductivity relaxation (ECR) method (Wang et al., 2012). CeO_2 powder was prepared using the carbonate coprecipitation method with cerium nitrate hexahydrate [$Ce(NO_3)_3 \cdot 6H_2O$, ≥99. 9%] as the precursors (Ding et al., 2008). The powder was uniaxially dry pressed under 320 MPa into rectangular bars and sintered at 1, 550°C for 5 h in air. The bar density was 96. 8%, measured using the Archimedes method. The bar size was about 30. 0 × 5. 20 × 0. 52 mm^3 . Ni film was deposited on the bar surface using nickel target (4 N purity, Kejing Materials Technology) by a sputter coater (JFC-1600, JEOL) at 20 mA and under a vacuum of 8 Pa. Afterwards, the bar was heated at a rate of 3°C min^{-1} to 800°C for 2 h in reducing atmosphere to form Ni particles on the bar surface. The deposition was conducted for 20, 40, and 80 s to vary the film thickness and, consequently, the amount of Ni particles per unit area. The surface microstructures were revealed using scanning electron microscopy (SEM, JSM-6700F, JEOL). The area covered by the Ni particles and the length of $Ni–CeO_2$ boundary were statistically determined using software Image J. The ECR experiments were conducted at 800°C with a digital multimeter (2001-785D, Keithley) using the four-probe technique (Wang et al., 2012). The atmosphere was switched from H_2 /Ar (5: 95) to H_2 /Ar (10: 90) to simulate the H_2 oxidation reaction. The gas was humidified within a

moisture bottle at room temperature, containing about 3% H_2O, and the gas flowing rate was 200 ml min $^{-1}$.

Temperature Programmed Desorption/Reduction Tests

The reaction kinetics was further investigated using H_2-temperature programmed desorption (TPD), which was performed using Thermo Electron Corporation TPDRO1100 flow apparatus. The H_2 consumption was measured by a TCD detector. Before the TPD test, a pretreatment process for CeO_2 and Ni–CeO_2 bars was carried out using H_2/N_2 (5: 95) gas mixture from room temperature to 150°C. Then, TPD signal was recorded while the samples were blown with N_2 at a flux of 20 ml min $^{-1}$ and heated from room temperature to 1, 000°C with a heating rate of 10°C min $^{-1}$.

Electrochemical Measurement

The electrochemical performance was investigated using symmetrical cells composed of YSZ (8 mol% yttria-stabilized zirconia) as the electrolyte substrates and porous CeO_2 impregnated with 8 wt% NiO as the electrodes. Dense YSZ substrates were fabricated by uniaxially pressing the 8 wt% YSZ powder (TZ-8Y, Tosoh Co., Japan) under 320 MPa followed by sintering at 1, 500°C for 5 h in air. Porous CeO_2 was prepared using printing and sintering processes. The CeO_2 slurry was prepared by mixing the CeO_2 powder with α-terpineol as solvent and ethyl cellulose as the binder. The slurry was printed on both sides of the YSZ substrates and then heated with the substrates at 1, 100°C for 2 h to form symmetric structures with the YSZ electrolyte sandwiched in two porous CeO_2 layers. Nickel was deposited by impregnation process. Ni(NO_3)$_2$ (≥99. 9%) was dissolved in a mixture of

water and ethanol (1: 1 volume ratio) with a concentration of 0. 5 mol L $^{-1}$. The solution was dropped on the porous electrodes, dried and heated at 800°C in air for 1 h to form NiO particles within the porous CeO_2 backbones. NiO was *in situ* reduced to Ni and thus forming the Ni–CeO_2 cermet electrodes. The volume ratio of Ni to CeO_2 was 5. 5: 100. The Solartron Frequency Response Analyzer 1260 and a Solartron Electrochemical Interface 1287 were used for electrochemical measurements. Ag paste (SRISR DAD-87) was used as electron collector layer, and Ag wires (≥99. 9%, Xiyu Electrical and Mechanical Technology) were used to ensure the electronic contact. The frequency range used was from 10^6 to 10^{-2} Hz, and the AC amplitude is 10 mV. The impedance was measured in humidified H_2 (~3% H_2O).

Results and Discussion

Electron Redistribution at Ni_{10}-CeO_2 (111) by Computation

A previous study has revealed that the trigonal pyramid-shaped Ni_{10} cluster with T_d symmetry is the most stable structure (Lu et al., 2011 ; Song et al., 2011 ; Rodríguez-Kessler and Rodríguez-Domínguez, 2015), and the low-index (111) surface of CeO_2 is the most stable surface, so that CeO_2 (111) surface is selected as the substrate to represent CeO_2 (Conesa, 1995). To simplify the calculation process, the effect of electrochemical environment such as potential is not considered in this work since the real reaction condition is too complicated to simulate precisely. Similar to previous studies of the metal–CeO_2 systems, we focus on the effect of heterogeneous structure of the CeO_2-supported metals, while the diffusion of metal

particles is not considered (Kim and Henkelman, 2012 ; Kim et al., 2012 ; Kishimoto et al., 2014 ; Liu et al., 2016). Based on this, the pyramid-shaped Ni_{10} cluster is constructed on the CeO_2 (111) surface to illustrate the properties of Ni–CeO_2 cermet for the H_2 reaction process. Various positions for Ni_{10} cluster on CeO_2 (111) surface are investigated, and the configuration with the lowest energy is displayed in Figure 1 , which will be used as the model to study the reaction process.

FIGURE 1

The side and top views of the optimized geometry structure of(A)the free-standing Ni_{10} cluster and(B)the optimized Ni_{10} cluster placed on the stoichiometric CeO_2 (111) with the lowest energy configuration. The dark blue, light yellow, and red balls refer to Ni, Ce, and O atoms, respectively. Numbers 1–5 refer to interface oxygen while 6–11 to surface oxygen.

The interaction between Ni_{10} cluster and CeO_2 (111) substrate is essential to elucidate the H_2 oxidation pathways and electrochemical catalytic properties since the charge transfer between Ni_{10} and CeO_2 (111) determines the chemical activity of the substrate to a great extent. Bader charge analysis indicates that ~1. 07 electrons are transferred from Ni_{10} cluster to CeO_2 (111) surface (Supplementary Figure 1). The redistributed charge density [i. e., the charge density difference between CeO_2 (111) with and without Ni_{10} cluster, is displayed in Figure 2]. It is found that the valence states of four Ce ions are reduced from Ce^{4+} to Ce^{3+} with three Ce ions under the Ni_{10} cluster and one adjacent to Ni_{10} cluster (Figures 2A–D).

Such remarkable charge transfer from Ni $_{10}$ cluster to CeO $_2$ (111) surface indicates that there is a strong interaction at the interface between Ni $_{10}$ cluster and CeO $_2$ (111) surface, resulting in a partially positively charged Ni $_{10}$ cluster on negatively charged CeO $_2$ (111) surface. Such structure also indicates that Ni can facilitate the formation of oxygen vacancy on the ceria surface.

FIGURE 2

Charge density difference profiles for Ni $_{10}$ -CeO $_2$ (111)(A–D)without and(E–H)with oxygen vacancy. The views without vacancy are(A)from top to bottom,(B)from bottom to top, and(C, D)side. The views with an interface oxygen vacancy (V4) are(E, F)while(G, H)refer to surface oxygen vacancy (V10). The views(E, G)are from top to bottom while(F, H)from bottom to top. The dark blue, light yellow, red balls, and black dotted circle refer to Ni, Ce, O atoms, and oxygen vacancy, respectively. The isosurface value is 0. 004 a. u. The yellow and blue colors refer to the positive and negative values, respectively.
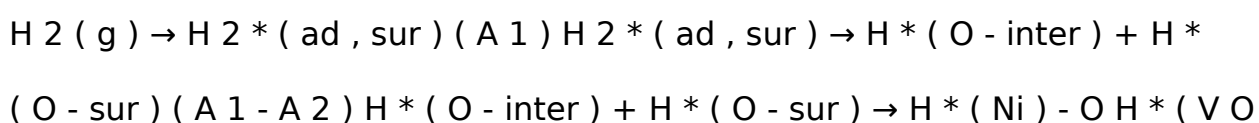
It is known that oxygen defects may alter the electronic structure and thus influence the H $_2$ oxidation reaction (Wu et al., 2015). Similar to previously reported configurations (Shishkin and Ziegler, 2010a , b), two types of oxygen vacancies are investigated (Supplementary Figure 2). The first type is the interface oxygen vacancy (labeled as V $_4$), created by removing one oxygen atom at the interface of Ni $_{10}$ and CeO $_2$. The second type is the surface oxygen vacancy (labeled as V $_{10}$), formed by removing one oxygen
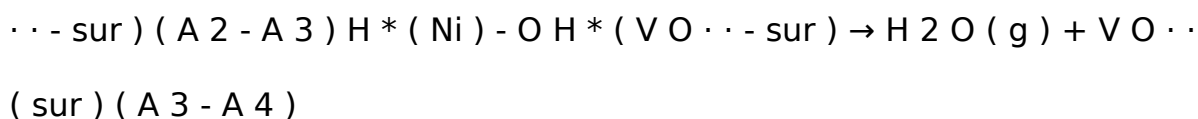
atom at the CeO$_2$ surface away from Ni$_{10}$. For model V$_4$, the Bader charge analysis indicates that about 0. 93 electrons are transferred from the Ni$_{10}$ cluster to the CeO$_2$ surface, which is smaller than that on the perfect CeO$_2$ (111) surface (1. 07 e). Although the presence of interface oxygen vacancy reduces the charge transferred from the Ni$_{10}$ cluster to the CeO$_2$ surface, still five Ce ions are found to be reduced to lower valences. As illustrated in Figures 2E, F, the transferred electrons are mainly located at two Ce ions neighboring to the Ni$_{10}$ cluster, and the remaining three Ce ions are underneath the Ni$_{10}$ cluster. However, for model V$_{10}$, more charges are transferred from the Ni$_{10}$ cluster to the reduced vacancy defect. The Bader charge analysis indicates that about 1. 58 electrons are transferred from Ni$_{10}$ cluster to the reduced CeO$_2$ (111) surface with surface oxygen vacancy (V$_{10}$), which is significantly larger than those on the perfect and oxygen-defected CeO$_2$ (111) surface with an interface oxygen vacancy. The plotted deformation charge density profiles, illustrated in Figures 2G, H, show that the transferred electrons are mainly situated on five reduced Ce ions adjacent to the Ni$_{10}$ cluster, and the reduced valence states of three Ce ions underneath the Ni$_{10}$ cluster are negligible. Therefore, both surface and interface oxygen vacancy significantly enhance the reduction in valence state of Ce ions on the surface. Besides, the electronic state of cerium, whether it is at the interface or surface, is obviously affected by the presence of nickel cluster under both conditions of oxygen-nonstoichiometric and perfect crystalline. Accordingly, the electrochemical performance on the ceria surface can be quite different from that at the Ni–ceria interface.

Computational Results of H_2 Oxidation Reaction Pathway on Ni_{10}-CeO_2 (111)

Since ceria itself is catalytically active to hydrogen oxidation, the reaction on the Ni–ceria system may proceed in two different situations, one on bare ceria and the other with involvement of Ni. The first pathway (pathway I) occurs on the bare ceria surface, which has been studied in our previous work (Wang et al., 2016). Briefly, pathway I starts with a relatively weak hydrogen adsorption on the oxide surface with the adsorption energy of -0.035 eV. H_2 prefers to be adsorbed in parallel with the stoichiometric CeO_2 (111) surface, subsequently dissociating into two hydrogen atoms over surface oxygen atoms while forming two hydroxyl groups by overcoming an energy barrier of 1. 073 eV. Finally, the two –OH species form an adsorbed water molecule and a residual oxygen vacancy with an energy barrier of 2. 399 eV, which is the most energy-consuming step.

The reaction processes with the participation of Ni are energetically preferred yet more complicated than that on the bare ceria surface. The initial step of hydrogen adsorption may happen either on ceria or Ni. In the first scenario where hydrogen is adsorbed on ceria, the possible reaction route (pathway II) is followed by disassociation of hydrogen molecule at the Ni–ceria interface and H_2O formation at 3PB as shown in the following steps A1–A4, where " sur" indicates ceria surface, and " inter" indicates the Ni–ceria interface.

$H 2 (g) \rightarrow H 2 * (ad , sur) (A 1) H 2 * (ad , sur) \rightarrow H * (O - inter) + H * (O - sur) (A 1 - A 2) H * (O - inter) + H * (O - sur) \rightarrow H * (Ni) - O H * (V O$

$\cdots$ - sur) (A 2 - A 3) H * (Ni) - O H * (V O $\cdots$ - sur) $\rightarrow$ H 2 O (g) + V O $\cdots$ (sur) (A 3 - A 4)
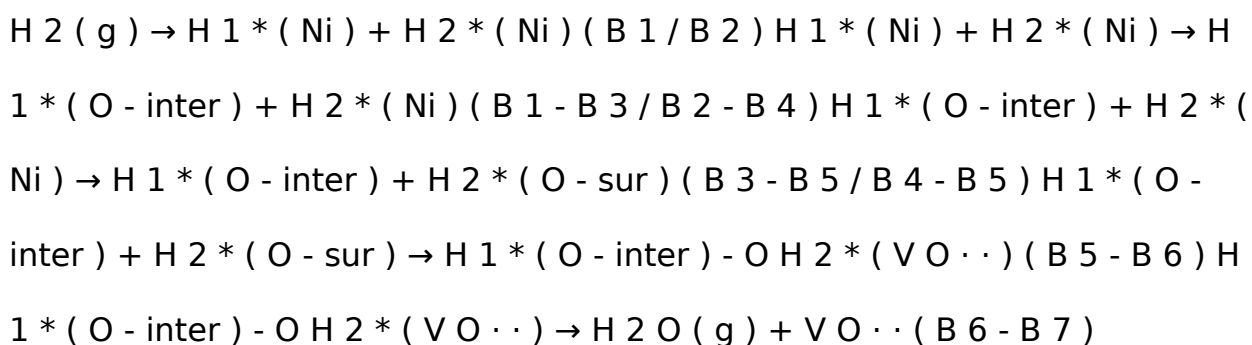
According to the calculated results displayed in Figure 3 for pathway II, the H $_2$ molecule is physically adsorbed on the ceria surface away from Ni in the first step (A1), with an adsorption energy of $-0. 538$ eV. The H–H bond length of the adsorbed H $_2$ molecule is 0. 754 Å (Supplementary Figure 3), slightly larger than the calculated equilibrium bond length of a free H $_2$ molecule (0. 740 Å) (Wang et al., 2016). Then, the adsorbed H $_2$ dissociates into two separated hydrogen atoms: one adsorbed on interface oxygen, and the other adsorbed on the surface oxygen (A1–A2). This step includes an energy barrier of 0. 876 eV, while the total energy difference from A1 to A2 is $-1. 710$ eV, indicating that the formation of two –OH species is exothermic. In the next step, the two adsorbed –OH species combines to form an adsorbed H $_2$ O on Ni $_{10}$ cluster by overcoming a high energy barrier of 1. 367 eV (A2–A3). The formation of adsorbed H $_2$ O is endothermic with an energy difference of 0. 629 eV. Finally, the adsorbed H $_2$ O molecule is released as gas phase by overcoming an energy barrier of 0. 969 eV. In short, the whole molecular pathway gives off 0. 650 eV, and the highest energy barrier of this exothermic reaction is 1. 367 eV, which is much smaller than 2. 399 eV for the H $_2$ oxidation reaction on the bare CeO $_2$ (111) (Wang et al., 2016).

FIGURE 3

Molecular pathway of H_2 oxidation reaction in Ni_{10}-CeO_2 (111) system with hydrogen adsorption on ceria surface and oxidation reaction at 3PB (pathway II).

In the second scenario, hydrogen is adsorbed on nickel rather than ceria in the initial step. According to a previous research, Ni not only functions as electron acceptor but also catalyzes the dissociation of hydrogen molecule into atoms. The hydrogen atoms formed on the Ni surface may spill over to the surface of oxides such as zirconia (Anderson and Vayner, 2006 ; Shishkin and Ziegler, 2009), LnO_x (Ln = Dy, Ho, Er, Yb, and Tb) (He et al., 2011), and gadolinia-doped ceria (Babaei et al., 2009).

The possible H-spillover pathway involves hydrogen adsorption and disassociation on Ni, hydrogen spillover, and water formation. The proposed steps are summarized as B1–B7.

$$H_2(g) \rightarrow H_1^*(Ni) + H_2^*(Ni) \quad (B_1/B_2)$$
$$H_1^*(Ni) + H_2^*(Ni) \rightarrow H_1^*(O\text{-}inter) + H_2^*(Ni) \quad (B_1\text{-}B_3/B_2\text{-}B_4)$$
$$H_1^*(O\text{-}inter) + H_2^*(Ni) \rightarrow H_1^*(O\text{-}inter) + H_2^*(O\text{-}sur) \quad (B_3\text{-}B_5/B_4\text{-}B_5)$$
$$H_1^*(O\text{-}inter) + H_2^*(O\text{-}sur) \rightarrow H_1^*(O\text{-}inter)\text{-}O H_2^*(V_O^{\cdot\cdot}) \quad (B_5\text{-}B_6)$$
$$H_1^*(O\text{-}inter)\text{-}O H_2^*(V_O^{\cdot\cdot}) \rightarrow H_2O(g) + V_O^{\cdot\cdot} \quad (B_6\text{-}B_7)$$

Because H_2O may form either at the ceria surface or at 3PB of Ni–ceria–gas interface, two possible H-spillover pathways are distinguished as illustrated in Figure 4 . Pathway III is labeled with black line, which proceeds with steps of B1, B3, and B5–B7, while red line refers to pathway IV that goes through B2, B4, and B5–B7. Both initial structures are dissociated H_2 molecule on the
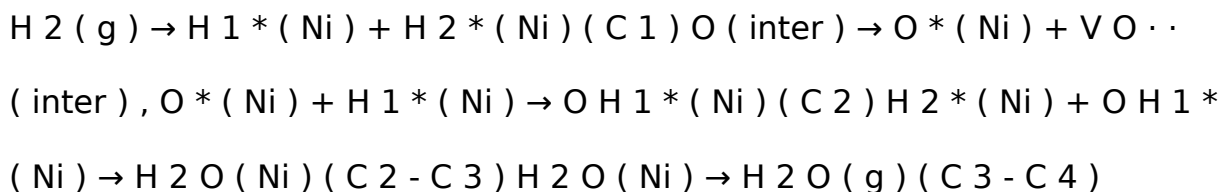
Ni $_{10}$ cluster surface (B1/B2). In pathway III, one dissociative H (H ^{1}) atom is adsorbed on the edge between the top and interlayer of Ni $_{10}$ cluster, while the other H (H ^{2}) atom is adsorbed on the edge between the interlayer and contact layer of Ni $_{10}$ cluster (B1). Then, H ^{1} slightly moves and combines with an interface oxygen near the Ni $_{10}$ cluster, while H ^{2} spills over to the ceria surface away from the Ni $_{10}$ cluster to combine with a surface oxygen. Thus, two hydroxyl groups are generated in this process, overcoming an energy barrier of 0. 853 eV (B3–B5). After that, H ^{1} is attracted to the hydroxyl group containing H ^{2} , forming one H $_2$ O molecule (B5–B6) and a surface oxygen vacancy (B6–B7) with energy barriers of 0. 662 and 0. 885 eV, respectively. In pathway IV, H atoms are adsorbed on two edges between the interlayer and the contact layer of Ni $_{10}$ cluster in structure B2, which is slightly more stable than structure B1. In the following steps, H atoms migrate from the Ni $_{10}$ cluster to the ceria surface and react with the oxygen atoms at interface and surface to form two –OH species, overcoming the energy barriers of 1. 302 and 1. 713 eV, respectively. In general, pathway III (black line) is more favorable compared to pathway IV (red line), since the highest energy barrier for pathway III (0. 885 eV for B6–B7) is much lower than that for pathway IV (1. 713 eV for B4–B5).

FIGURE 4

The H-spillover pathways of H $_2$ oxidation in the Ni $_{10}$ -CeO $_2$ (111) system with hydrogen adsorption on Ni $_{10}$ and oxidation reaction at 3PB (pathway III in black lines and pathway IV in red lines).

The possible O-spillover pathways include hydrogen adsorption and dissociation on Ni, oxygen spillover from ceria to Ni cluster, and formation of H_2O molecule, summarized as C1–C4 and illustrated in <u>Figure 5A </u>for pathway V.

$$H_2(g) \rightarrow H1*(Ni) + H2*(Ni) \quad (C1)$$
$$O(inter) \rightarrow O*(Ni) + V_O^{\cdot\cdot}(inter),$$
$$O*(Ni) + H1*(Ni) \rightarrow OH1*(Ni) \quad (C2)$$
$$H2*(Ni) + OH1*(Ni) \rightarrow H_2O(Ni) \quad (C2-C3)$$
$$H_2O(Ni) \rightarrow H_2O(g) \quad (C3-C4)$$

The initial structure C1 is for the disassociation of hydrogen molecule. In the following step, an oxygen atom at the Ni_{10}-CeO_2 interface spill overs from the oxide surface toward the metal cluster, then reacts with the hydrogen atom to form a hydroxyl group while leaving an interface oxygen vacancy (C1–C2). This is the most energy-consuming step, as it contains the highest energy barrier of 1. 876 eV. Next, the hydroxyl group reacts with H atom, forming an adsorbed H_2O on the Ni_{10} cluster by overcoming an energy barrier of 0. 970 eV (C2–C3). In the final step, it consumes 0. 762 eV to release the adsorbed H_2O molecule to the gas phase. As a whole, this O-spillover process is endothermic with a negligible energy of 0. 003 eV, and the rate-limiting process is H_2 oxidation.

FIGURE 5

The O-spillover pathways of H_2 oxidation in the Ni_{10}-CeO_2 (111) system with hydrogen adsorption on Ni_{10} and oxidation reaction at 3PB:(A)pathway V for the stoichiometric structure and(B)pathway VI for nonstoichiometric structure with a surface oxygen vacancy.

Besides, the situation where an oxygen vacancy is created on the ceria surface is also considered, as illustrated in Figure 5B for pathway VI. In this case, the adsorption energy for the first step (H_2 disassociation on Ni_{10} cluster) is −1. 592 eV, which is less stable than the C1 structure. Next, interface O atom migrates to the Ni surface and reacts with one H atom to form an –OH species by overcoming a large energy barrier of 2. 035 eV. Doubtlessly, it takes more energy to achieve a O-spillover step when a surface oxygen vacancy exists on the ceria.

In conclusion, six possible pathways are proposed for the oxidation reaction on the Ni–ceria system. Pathway I takes place on the bare ceria surface and is entirely unrelated to the Ni–ceria interface. The other five pathways are all 3PB related since the reaction steps are either linking directly to the interface oxygen atoms (positions 1–5 in Figure 1) or to the surface oxygen atoms (positions 6–11 in Figure 1), noting that surface atoms are also affected by the nickel cluster as mentioned in the previous discussion. In addition, the surface atoms in our Ni–CeO_2 (111) model at the atomic scale could be regarded as the interface atoms in real electrochemical system, since the electrode is often characterized in a much larger scale such as nanoscale. Thus, it is reasonable to treat pathways II–VI as the possible reaction processes for the hydrogen oxidation reaction at the Ni–ceria interface while only pathway I as the pathway on the ceria surface.

Table 1 lists the hydrogen adsorption energy, highest energy barrier, and total energy balance of each pathway. The hydrogen adsorption energy differs enormously depending on the location. The energy for adsorption on

bare ceria in pathway I is only -0.035 eV, while the adsorption energy in the Ni_{10} cluster in pathways III, IV, and V are around -1.9 eV. Besides, the adjacent Ni_{10} cluster in pathway II promptly increases the adsorption energy on the surface site, from -0.035 to -0.538 eV. Thus, the enhancement of hydrogen adsorption by Ni particles is quite obvious. Among the five pathways related to the Ni–ceria interface, the molecular pathway (pathway II) and the two H-spillover pathways (pathways III and IV) are all finished with formation of a surface oxygen vacancy rather than interface oxygen vacancy. Energetically speaking, pathway III is more favored than pathways II and IV. The highest energy barrier in pathway III is only 0.885 eV, about two-thirds of pathway II and one-half of pathway IV, while the energy balance is the lowest, -0.875 eV. In contrast, the highest energy barriers in pathways V and VI proceeding with oxygen spillover are more than twice as large as that in pathway III. Besides, the energy balance of pathway V (0.003 eV) is contradictory to the thermodynamic prediction. Consequently, the oxygen spillover pathways rarely contribute to the overall anodic reaction, as they are unlikely to occur.

TABLE 1

Adsorption energy and highest energy barrier for H_2 oxidation reaction at Ni_{10}-CeO_2 (111) *via* various pathways.

It is noted that the mechanism of hydrogen oxidation for Ni–CeO_2 system is quite different from that for Ni–YSZ system, although both are controlled by the reaction at 3PB. For Ni–YSZ, the energetically favored pathway is

hydrogen spillover from Ni to the Ni–YSZ interface with formation of an interface vacancy, while hydrogen spillover from the interface to YSZ surface with formation of a surface vacancy is very unfavorable because interfacial vacancy formation is much easier than the latter (Shishkin and Ziegler, 2014). However, due to facile formation of the surface vacancy at the CeO_2 (111) surface, the hydrogen oxidation for the Ni–CeO_2 system tends to proceed with hydrogen spillover to the CeO_2 (111) surface and finish with the formation of a surface oxygen vacancy. This result is obvious for the energetically most favored route (pathway III).

As a result, assumption could be made that the reaction rate for interface process that mainly occurs following pathway III should be much higher than that for the ceria surface of pathway I, although both of them could exist in practical situations. Besides, the contribution from the surface reaction to the total electrode reaction could be very small, and the total reaction rate may be controlled by the interface length (i. e., the length of 3PB). The surface and interface reaction rates and their contributions will be further compared in *Experimental* , with the perspective of reaction kinetics.

Experimental Results and Discussion
The hydrogen oxidation reaction catalyzed by ceria can be represented using Kroger–Vink notations as

$$H_2(g) + O_O^\times + 2 Ce_{Ce}^\times (Ce+4) \rightarrow H_2O(g) + V_O^{\cdot\cdot} + 2 Ce_{Ce}^\prime (Ce+3) \quad (2)$$
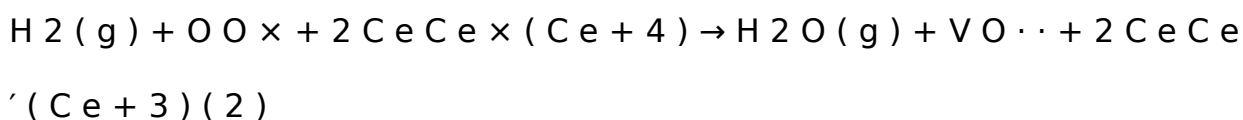
Equation (2) can also be considered as the ceria reduction reaction. Comparing Equations (1, 2), it is found that the ceria reduction reaction is equivalent to the anodic H $_2$ oxidation reaction (Wang et al., 2012). Thus, ECR method is adopted to simulate the anodic reaction. By increasing the H $_2$ partial pressure, the equilibrium in Equation (2) shifts toward the right. Meanwhile, Ce $^{4+}$ is reduced to Ce $^{3+}$, and the conductivity increases. The conductivity change is tested with dense bar samples.

The CeO $_2$ bar consists of grains several micrometers in size (Figure 6A). When Ni is deposited, the surface clearly presents fine particles (Figure 6B). These fine particles are Ni as formed in the sputtering–heating process, in which the sputtering results in a thin nickel film while the heating turns the film into particles. The fine particles are isolated and evenly distributed. The non-connected Ni particles do not influence the ground conductivity of the ceria bar. The Ni particle number per unit area increases with the sputtering time (Supplementary Figure 4). The diameter and vertical height of Ni particles are about 20 and 13 nm, respectively, as shown from the three-dimensional AFM pictures (Figures 6C, D).

FIGURE 6

Surface micrographs for(A)scanning electron microscopy (SEM) view of a bare CeO $_2$ bar,(B)SEM,(C)atomic force microscopy (AFM), and(D)three-dimensional AFM pictures for the bar with Ni particles prepared by 40 s deposition.

Figure 7 shows the curves of normalized conductivity measured at 800°C. The surface H_2 oxidation reaction rate for the bare CeO_2 is very slow as the re-equilibrium time is over 12, 000 s, which is much longer than that of doped ceria, about 7, 000 s (Wang et al., 2013). When Ni particles are deposited on the ceria surface, however, the re-equilibrium time is sharply reduced. Besides, the re-equilibrium appears to be faster for the sample with longer deposition time of Ni. The re-equilibrium times for samples with 20, 40, and 80 s deposition are 2, 171, 1, 520, and 426 s, respectively. The accelerated re-equilibrium demonstrates enhanced surface reaction kinetics caused by Ni particles. The process of conductivity relaxation consists of the surface reaction to form oxygen ion vacancy and bulk diffusion of oxygen ions. Since the reaction is dominated by the surface process, the ECR data can be fitted with following formula (Yasuda and Hikita, 1994 ; Wang et al., 2013).

$$\frac{\sigma(t) - \sigma(0)}{\sigma(\infty) - \sigma(0)} = 1 - \exp\left(-\frac{k_{chem} t}{a}\right) \quad (3)$$

where k_{chem} is the chemical surface exchange coefficient, which quantitatively represents the reaction rate of Equation (1), and the fitted k_{chem} values are listed in Supplementary Table 1 . $\sigma(0)$ and $\sigma(\infty)$ are the equilibrated conductivities at the initial and final time of the relaxation curve. a is a constant and numerically equals half of the bar sample thickness. k_{chem} is 0.72×10^{-5} cm s^{-1} for the bare CeO_2 at 800°C, which equals to the reaction rate constant for hydrogen reduction on ceria surface, k_{ceria} . When Ni sputter is conducted for 20, 40, and 80 s, the k_{chem} dramatically increases to 6.03×10^{-5} , 10.3×10^{-5} , and 39.1×10^{-5} cm s^{-1} ,

respectively, proving that the surface reaction rate is remarkably accelerated by the involvement of Ni particles.

FIGURE 7

Normalized conductivity curves vs. relaxation time for bare CeO_2 and CeO_2 with Ni particles, which are prepared by 20, 40, and 80 s deposition.

Physically, k_{chem} is contributed by the reaction on the bare ceria surface and the reaction related to the Ni particles, k_{Ni} (Wu et al., 2015)

$$k_{Ni} = k_{chem} - K_{ceria} (1 - \theta) \quad (4)$$

k_{Ni} represents the nickel effect on the reaction, θ is the surface coverage of the Ni particles and $(1 - \theta)$ is surface fraction of the bare ceria (Supplementary Table 1). Figure 8 shows k_{Ni} as a function of θ and L_{3PB} , the length of Ni–CeO_2 interface (i. e., the length of 3PB boundaries). k_{Ni} increases linearly with L_{3PB} , suggesting that k_{Ni} represents the reaction that is limited by the step occurring at/near the Ni–CeO_2 interface rather than on the Ni–gas surface. According to the DFT analysis, the hydrogen reduction reactions are mostly favored by hydrogen-spillover-based pathway III, which is also limited to the Ni–CeO_2 -gas 3PB. Thus, the DFT approach agrees well with the ECR conclusion that the Ni-related reaction mainly occurs at/near the Ni–CeO_2 -gas 3PB.

FIGURE 8

k_{Ni} as a function of(A)density of 3PB (L_{3PB}) and(B)surface coverage of Ni particles, (θ).

According to the discussion based on DFT calculation, both reactions at the Ni-ceria interface and on the ceria surface may contribute to the H_2 oxidation. Under the ECR experimental conditions, the reaction rate constant k_{Ni} for H_2 oxidation at the interface is much higher than that on the ceria surface k_{ceria} (Supplementary Table 1). In addition, k N i k c e r i a increases with L_{3PB} since a higher 3PB density means more active sites for the catalytic reaction. The highest k N i k c e r i a value is about 53, demonstrating that the interface reaction is dominant although surface reaction exists. The ECR derived faster reaction rate at the interface than on the surface and is well-supported by the lower energy barrier in pathway III than pathway I as obtained by the DFT calculation.

The hydrogen adsorption/desorption on the ceria surface and Ni–ceria interface is compared with hydrogen-TPD measurement (Figure 9). The desorption curve for bare ceria shows only one desorption peak, which shows that the hydrogen desorption/adsorption on the ceria surface begins at about 450°C and reaches its highest rate at 725°C. Quite differently, the curve for the Ni-ceria includes two additional peaks at 408 and 520°C. These two peaks must be attributed to the adsorption on Ni particles. The additional adsorption on Ni as demonstrated with TPD analysis is well-consistent with the high adsorption energy for Ni $_{10}$ -CeO $_2$ (111) obtained from DFT calculation.

FIGURE 9

Hydrogen temperature programmed desorption profiles for CeO_2 and Ni–CeO_2 powders.

The electrochemical performance is compared with symmetrical cell using YSZ as the electrolyte substrates. Figure 10 shows the impedance spectra measured at 800°C, where the response corresponding to the ohmic resistance is deducted to compare the electrode response clearly. The interfacial polarization resistance is 3. 18 and 0. 88 $\Omega\,cm^2$ for the ceria and Ni-ceria electrodes, respectively. The reaction at the porous ceria electrode takes place at the ceria surface, while the Ni-ceria electrode provides additional reaction sites at the Ni-ceria interface. Since only 5. 5% Ni is infiltrated to porous ceria to form the Ni-ceria electrode, the difference in electrode polarization resistance could roughly be attributed to the interface considering that the two electrodes have almost the same electronic conductivities and pore structures. Thus, the presence of the Ni-ceria interface in this work improves the electrochemical performance by 72. 3%, proving that 3PB dominates the electrode reaction on Ni-ceria cermet anodes, which is possibly associated with the improved hydrogen adsorption capability and reduced energy barrier for hydrogen reduction.

FIGURE 10

Impedance spectra measured at 800°C.

Conclusion

Both theoretical calculations and experiments are conducted regarding Ni–CeO_2 as anode material for SOFCs. Via DFT + U computations, charge transfer between Ni_{10} cluster and CeO_2 (111) surface proves the synergistic effects existing in the Ni-ceria system. Then, five possible hydrogen oxidation pathways over the Ni–CeO_2 electrode are proposed, including different sites for adsorption and reaction to evaluate the effects of Ni on CeO_2 (111) surface. The results demonstrate that nickel can largely enhance H_2 adsorption on the ceria surface and lowers the energy barrier for disassociated hydrogens to combine with a surface oxygen of CeO_2 and form H_2O. The highest energy barrier decreases from 2. 399 eV on pure CeO_2 to 0. 885 eV at the Ni–CeO_2 interface in pathway III with hydrogen spillover mechanism, which can be concluded as the most energetically favored pathway. Furthermore, experimental results are found to be consistent with the theoretical calculations. ECR experiments demonstrate that surface reaction rate k_{Ni} increases linearly with the density of 3PB, and 98% of the total hydrogen oxidation is contributed by interface reaction at 3PB. H_2-TPD measurements also show enhanced hydrogen adsorption caused by Ni, as two additional and stronger desorption peaks appear at lower temperatures compared to bare ceria. Finally, EIS of ceria and Ni-ceria electrodes are measured to compare the electrochemical performance. The interfacial polarization resistance is remarkably reduced from 3. 18 Ω cm^2 for pure ceria electrode to 0. 88 Ω cm^2 for Ni-ceria electrode at 800°C.

Data Availability Statement

The original contributions presented in the study are included in the article/

Supplementary Materials , further inquiries can be directed to the

corresponding author/s.

Author Contributions

CX and XW conceived of the idea, designed the calculations and

experiments, and analyzed the data. YJ and MZ carried out the

electrochemical experiments. JX conducted the characterizations. SW

performed the theoretical calculations. YY participated in the discussion of

the results. YJ and SW wrote the paper. All authors commented on the

manuscript.

Funding

Conflict of Interest

Acknowledgments

Supplementary Material

The Supplementary Material for this article can be found online at: https://www. frontiersin. org/articles/10. 3389/fchem. 2020. 591322/full#supplementary-material

References

Anderson, A. B., and Vayner, E. (2006). Hydrogen oxidation and proton transport at the Ni–zirconia interface in solid oxide fuel cell anodes: quantum chemical predictions. *Solid State Ionics* 177, 1355–1359. doi: 10. 1016/j. ssi. 2006. 05. 032

Andersson, D. A., Simak, S., Johansson, B., Abrikosov, I., and Skorodumova, N. V. (2007). Modeling of ce o 2, ce 2 o 3, and ce o 2– x in the lda+ u formalism. *Phys. Rev. B* 75: 035109. doi: 10. 1103/PhysRevB. 75. 035109

Babaei, A., Jiang, S. P., and Li, J. (2009). Electrocatalytic promotion of palladium nanoparticles on hydrogen oxidation on Ni/GDC anodes of SOFCs via spillover. *J. Electrochem. Soc.* 156, B1022–B1029. doi: 10. 1149/1. 3156637

Blochl, P. E., Jepsen, O., and Andersen, P. (1994). Improved tetrahedron method for Brillouin-zone integrations. *Phys. Rev. B Condensed Matter* 49, 16223–16233. doi: 10. 1103/PhysRevB. 49. 16223

Conesa, J. (1995). Computer modeling of surfaces and defects on cerium dioxide. *Surface Sci.* 339, 337–352. doi: 10. 1016/0039-6028(95)00595-1

Cucinotta, C. S., Bernasconi, M., and Parrinello, M. (2011). Hydrogen oxidation reaction at the Ni/YSZ anode of solid oxide fuel cells from first principles. *Phys. Rev. Lett.* 107: 206103. doi: 10. 1103/PhysRevLett. 107. 206103

Ding, D., Liu, B., Zhu, Z., Zhou, S., and Xia, C. (2008). High reactive Ce0. 8Sm0. 2O1. 9 powders via a carbonate co-precipitation method as electrolytes for low-temperature solid oxide fuel cells. *Solid State Ionics* 179, 896–899. doi: 10. 1016/j. ssi. 2007. 11. 015

Fergus, J. W. (2006). Electrolytes for solid oxide fuel cells. *J. Power Sources* 162, 30–40. doi: 10. 1016/j. jpowsour. 2006. 06. 062

Hahn, K. R., Seitsonen, A. P., Iannuzzi, M., and Hutter, J. (2015). Functionalization of CeO2 (1 1 1) by deposition of small Ni clusters: effects on CO $_2$ adsorption and O vacancy formation. *ChemCatChem* 7, 625–634. doi: 10. 1002/cctc. 201402906

Hammer, B., Hansen, L. B., and Nørskov, J. K. (1999). Improved adsorption energetics within density-functional theory using revised Perdew-Burke-

Ernzerhof functionals. *Phys. Rev. B* 59: 7413. doi: 10. 1103/PhysRevB. 59. 7413

He, B., Wang, W., Zhao, L., and Xia, C. (2011). Ni–LnOx (Ln= Dy, Ho, Er, Yb and Tb) cermet anodes for intermediate-temperature solid oxide fuel cells. *Electrochim. Acta* 56, 7071–7077. doi: 10. 1016/j. electacta. 2011. 05. 117

Horita, T., Kishimoto, H., Yamaji, K., Xiong, Y., Sakai, N., Brito, M. E., et al. (2006). Materials and reaction mechanisms at anode/electrolyte interfaces for SOFCs. *Solid State Ionics* 177, 1941–1948. doi: 10. 1016/j. ssi. 2006. 01. 013

Kašpar, J., Fornasiero, P., and Graziani, M. (1999). Use of CeO_2 -based oxides in the three-way catalysis. *Catalysis Today* 50, 285–298. doi: 10. 1016/S0920-5861(98)00510-0

Kim, H. Y., and Henkelman, G. (2012). CO oxidation at the interface between doped CeO_2 and supported Au nanoclusters. *J. Phys. Chem. Lett.* 3, 2194–2199. doi: 10. 1021/jz300631f

Kim, H. Y., Lee, H. M., and Henkelman, G. (2012). CO oxidation mechanism on CeO_2 -supported Au nanoparticles. *J. Am. Chem. Soc.* 134, 1560–1570. doi: 10. 1021/ja207510v

Kishimoto, H., Suzuki, A., Shimonosono, T., Nishi, M., Yamaji, K., Brito, M. E., et al. (2014). Effect of the oxide substrate on the nickel particle properties. *Solid State Ionics* 262, 403–406. doi: 10. 1016/j. ssi. 2014. 01. 004

Kresse, G., and Furthmüller, J. (1996). Efficient iterative schemes for ab initio total-energy calculations using a plane-wave basis set. *Phys. Rev. B* 54: 11169. doi: 10. 1103/PhysRevB. 54. 11169

Kümmerle, E., and Heger, G. (1999). The structures of C–$Ce_2O_3 + \delta$, Ce_7O_{12}, and $Ce_{11}O_{20}$. *J. Solid State Chem.* 147, 485–500. doi: 10. 1006/jssc. 1999. 8403

Laosiripojana, N., Sutthisripok, W., and Assabumrungrat, S. (2005). Synthesis gas production from dry reforming of methane over CeO_2 doped Ni/Al_2O_3: influence of the doping ceria on the resistance toward carbon formation. *Chem. Eng. J.* 112, 13–22. doi: 10. 1016/j. cej. 2005. 06. 003

Liu, B., Zhao, Z., Henkelman, G., and Song, W. (2016). Computational design of a CeO_2-supported Pd-based bimetallic nanorod for CO oxidation. *J. Phys. Chem. C* 120, 5557–5564. doi: 10. 1021/acs. jpcc. 6b00253

Lu, Q. L., Luo, Q., Chen, L., and Wan, J. (2011). Structural and magnetic properties of Ni_n ($n = 2$–21) clusters. *Eur. Phys. J.* 61, 389–396. doi: 10. 1140/epjd/e2010-10129-8

Nolan, M., Grigoleit, S., Sayle, D. C., Parker, S. C., and Watson, G. W. (2005). Density functional theory studies of the structure and electronic structure of pure and defective low index surfaces of ceria. *Surface Sci.* 576, 217–229. doi: 10. 1016/j. susc. 2004. 12. 016

Ormerod, R. M. (2003). Solid oxide fuel cells. *Chem. Soc. Rev.* 32, 17–28. doi: 10. 1039/b105764m

Perdew, J. P., Burke, K., and Ernzerhof, M. (1996). Generalized gradient approximation made simple. *Phys. Rev. Lett.* 77: 3865. doi: 10. 1103/PhysRevLett. 77. 3865

Ramirez-Cabrera, E., Atkinson, A., and Chadwick, D. (2000). The influence of point defects on the resistance of ceria to carbon deposition in hydrocarbon catalysis. *Solid State Ionics* 136, 825–831. doi: 10. 1016/S0167-2738(00)00507-5

Rodríguez-Kessler, P., and Rodríguez-Domínguez, A. (2015). Stability of Ni clusters and the adsorption of CH4: first-principles calculations. *J. Phys. Chem. C* 119, 12378–12384. doi: 10. 1021/acs. jpcc. 5b01738

Shishkin, M., and Ziegler, T. (2009). Oxidation of H2, CH4, and CO molecules at the interface between nickel and yttria-stabilized zirconia: a theoretical study based on DFT. *J. Phys. Chem. C* 113, 21667–21678. doi: 10. 1021/jp905615c

Shishkin, M., and Ziegler, T. (2010a). The electronic structure and chemical properties of a Ni/CeO2 anode in a solid oxide fuel cell: A DFT+ U study. *J. Phys. Chem. C* 114, 21411–21416. doi: 10. 1021/jp105316p

Shishkin, M., and Ziegler, T. (2010b). Hydrogen oxidation at the Ni/yttria-stabilized zirconia interface: a study based on density functional theory. *J. Phys. Chem. C* 114, 11209–11214. doi: 10. 1021/jp1030575

Shishkin, M., and Ziegler, T. (2014). Direct modeling of the electrochemistry in the three-phase boundary of solid oxide fuel cell anodes by density

functional theory: a critical overview. *Phys. Chem. Chem. Phys.* 16, 1798–1808. doi: 10. 1039/C3CP53943A

Song, W., Lu, W.-C., Wang, C., and Ho, K. (2011). Magnetic and electronic properties of the nickel clusters Nin (*n* < 30). *Comput. Theoret. Chem.* 978, 41–46. doi: 10. 1016/j. comptc. 2011. 09. 028

Sun, C., and Stimming, U. (2007). Recent anode advances in solid oxide fuel cells. *J. Power Sources* 171, 247–260. doi: 10. 1016/j. jpowsour. 2007. 06. 086

Wang, S., Zheng, M., Li, M., Wu, X., and Xia, C. (2016). Synergistic effects towards H $_2$ oxidation on the Cu–CeO $_2$ electrode: a combination study with DFT calculations and experiments. *J. Mater. Chem. A* 4, 5745–5754. doi: 10. 1039/C6TA00732E

Wang, Y., Wang, Y., and Xia, C. (2012). Surface process of doped ceria reduction by electrical conductivity relaxation. *J. Electrochem. Soc.* 159, F570–F576. doi: 10. 1149/2. 037209jes

Wang, Y., Zhu, Z., and Xia, C. (2013). Hydrogen oxidation at metal–ceria boundary by electrical conductivity relaxation method. *Electrochem. Commun.* 36, 10–13. doi: 10. 1016/j. elecom. 2013. 08. 026

Wu, X.-P., Gong, X.-Q., and Lu, G. (2015). Role of oxygen vacancies in the surface evolution of H at CeO $_2$ (111): a charge modification effect. *Phys. Chem. Chem. Phys.* 17, 3544–3549. doi: 10. 1039/C4CP04766D

Yasuda, I., and Hikita, T. (1994). Precise determination of the chemical diffusion coefficient of calcium-doped lanthanum chromites by means of electrical conductivity relaxation. *J. Electrochem. Soc.* 141, 1268–1273. doi: 10. 1149/1. 2054908